

Reflectance Prediction-based Knowledge Distillation for Robust 3D Object Detection in Compressed Point Clouds

Hao Jing, Anhong Wang, Yifan Zhang, Donghan Bu, and Junhui Hou, *Senior Member, IEEE*

Abstract—Regarding intelligent transportation systems for vehicle networking, low-bitrate transmission via lossy point cloud compression is vital for facilitating real-time collaborative perception among vehicles with restricted bandwidth. In existing compression transmission systems, the sender lossily compresses point coordinates and reflectance to generate a transmission code stream, which faces transmission burdens from reflectance encoding and limited detection robustness due to information loss. To address these issues, this paper proposes a 3D object detection framework with reflectance prediction-based knowledge distillation (RPKD). We compress point coordinates while discarding reflectance during low-bitrate transmission, and feed the decoded non-reflectance compressed point clouds into a student detector. The discarded reflectance is then reconstructed by a geometry-based reflectance prediction (RP) module within the student detector for precise detection. A teacher detector with the same structure as student detector is designed for performing reflectance knowledge distillation (RKD) and detection knowledge distillation (DKD) from raw to compressed point clouds. Our RPKD framework jointly trains detectors on both raw and compressed point clouds to improve the student detector’s robustness. Experimental results on the KITTI dataset and Waymo Open Dataset demonstrate that our method can boost detection accuracy for compressed point clouds across multiple code rates. Notably, at a low code rate of 2.146 Bpp on the KITTI dataset, our RPKD-PV achieves the highest mAP of 73.6, outperforming existing detection methods with the PV-RCNN baseline.

Index Terms—Compressed Point Clouds, 3D Object Detection, Knowledge Distillation, Reflectance Prediction.

I. INTRODUCTION

LIDAR point clouds, composed of sparse points with both geometric (coordinates) and attribute (reflectance) information about object surfaces, are vital for predicting

the categories, positions, and bounding boxes of 3D objects. In cooperative perception among networked vehicles, local vehicles (receivers) need to rapidly acquire LiDAR point clouds captured by neighboring vehicles (senders) to enable an expanded perception range and accurate object detection [1]–[4]. Raw point clouds are extremely voluminous and require a high transmission bandwidth, making it difficult to realize real-time cooperative perception. To this end, point cloud compression reduces the amount of transmitted data, improving data acquisition efficiency at the receiver. However, compressed point clouds generated by existing methods often lose some geometric coordinates and reflectance information, leading to suboptimal performance in 3D object detection. Therefore, enhancing the 3D detector’s robustness for compressed point clouds is of great research significance.

Existing 3D object detection methods in compressed point clouds can be classified into two categories based on their reflectance processing approaches: 3D object detection with or without reflectance encoding. For 3D object detection with reflectance encoding, the geometry-based point cloud compression (G-PCC) [5] separately compresses the coordinates and reflectance of voxelized point clouds to form geometry and attribute bitstreams for reconstruction and detection tasks, as shown in Fig. 1(a). Building on this, Unicorn [6], [7] introduces a learning-based compression framework that utilizes multiscale sparse tensors from single-frame voxelized point clouds and lower-scale priors from multi-frame point clouds to improve compression and reconstruction performance. However, these methods face a significant burden from the attribute bitstream during networking transmission, limiting transmission efficiency. To solve this issue, in 3D object detection without reflectance encoding, existing compression methods based on voxelized point clouds and deep learning [8]–[13] typically focus on compressing geometric coordinates while discarding reflectance to elevate transmission efficiency, as presented in Fig. 1(b). As an illustration, PCC-S [9] employs a geometric perception module to improve the learning of sibling and ancestor contexts in an octree structure for excellent geometric coordinates compression and reconstruction, during which the decoded data is termed non-reflectance compressed point clouds. However, lossy compression by these methods causes substantial information loss in low-bitrate transmission, severely impacting 3D object detection accuracy. To address these challenges, this paper aims to improve the transmission efficiency of lossy compressed point clouds and develop robust compressed point-cloud detectors, supported by a series of

This work was supported in part by the National Natural Science Foundation of China (U23A20314 and 62422118), in part by Industrial Application of Shanxi Provincial Technology Innovation Center (IVASXTIC2022), in part by Shanxi Province ‘Reveal the List’ Major Project (202301156401007), in part by Taiyuan Key Core Technology Research ‘Reveal the List’ Project (2024TYJB0128, 20240027), and in part by the Hong Kong Research Grants Council under Grants 11219324 and 11219422. (*Corresponding authors: Anhong Wang; Yifan Zhang.*)

Hao Jing, Anhong Wang, and Donghan Bu are with the School of Electronic Information Engineering, Taiyuan University of Science and Technology, No. 66 Waliu Road, Taiyuan 030024, China. (e-mail: b20201591001@stu.tyust.edu.cn; ahwang@tyust.edu.cn; b202115310021@stu.tyust.edu.cn).

Yifan Zhang is with the School of Mechatronic Engineering and Automation, Shanghai University, Shanghai, China, and is also with the Department of Computer Science, City University of Hong Kong, Hong Kong, China (e-mail: yfzhang@shu.edu.cn).

Junhui Hou is with the Department of Computer Science, City University of Hong Kong, Hong Kong, China (e-mail: jh.hou@cityu.edu.hk).

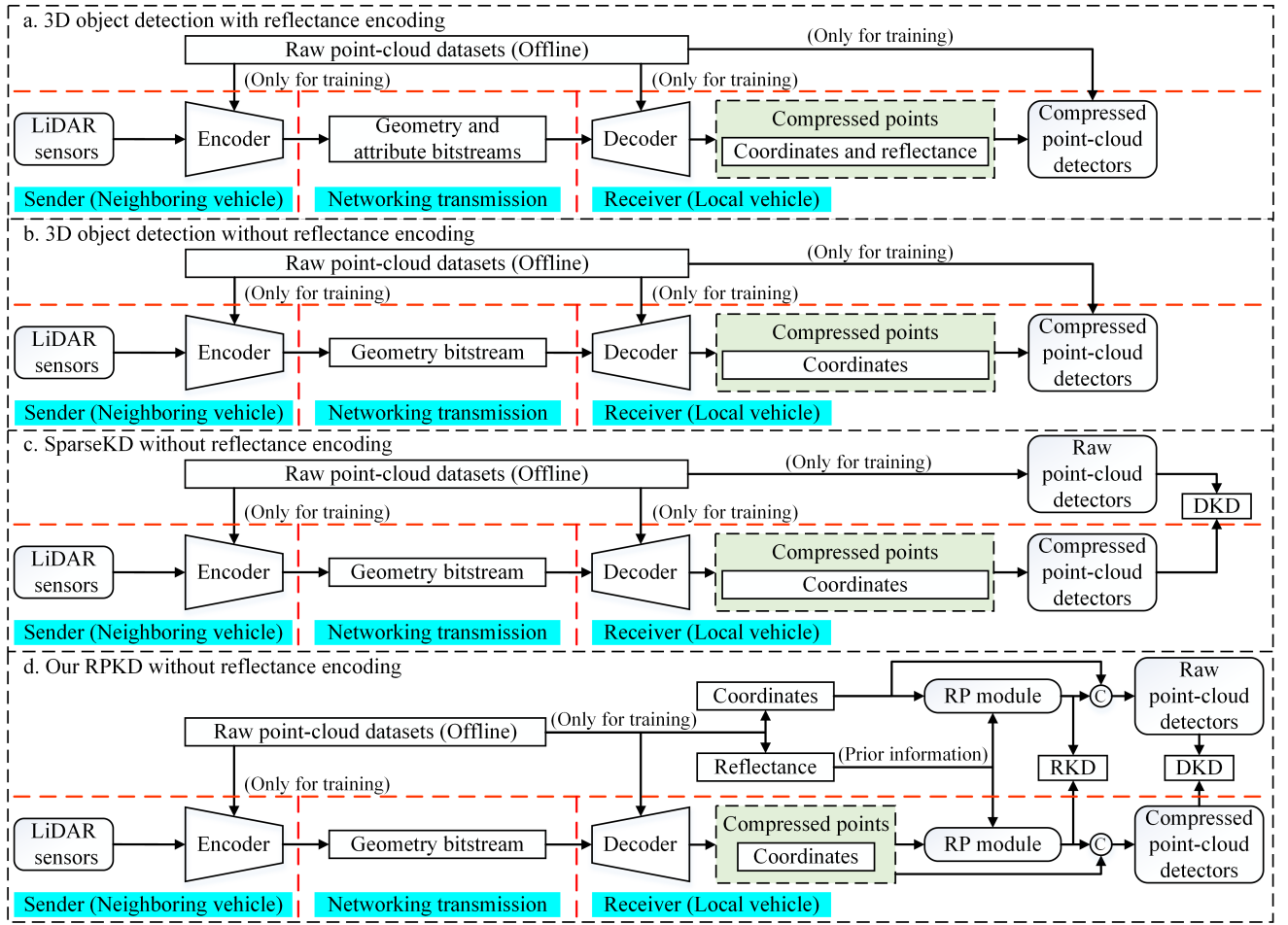


Fig. 1. Comparisons between our approach and previous methods in 3D object detection for compressed point clouds. (a) 3D object detection with reflectance encoding faces a significant transmission burden from the attribute bitstream. (b) To address this, 3D object detection without reflectance encoding elevates transmission efficiency by compressing only geometric coordinates. Both these methods exhibit limited detection robustness for lossy point cloud compression due to information loss. (c) In our reimplementation, SparseKD without reflectance encoding shows a slight performance improvement by distillation using accurate detection knowledge from raw point-cloud detectors, although it lacks crucial reflectance information. (d) Consequently, our RPKD without reflectance encoding introduces the RP module, RKD, and DKD constraints, remarkably enhancing detection performance for compressed point clouds.

detailed studies.

Fig. 1(c) shows a baseline of our method. It takes accurate object predictions from raw point clouds as teacher knowledge for distillation during detection training. In this setup, the teacher model transfers its knowledge to compressed point-cloud detectors through response-based detection knowledge distillation (DKD). As shown in Fig. 2, SparseKD-PV outperforms PV-RCNN by an average of 1.11% in mAP across multiple data types, whereas it still exhibits a significant detection performance gap compared to PV-RCNN’s mAP of 75.56 on raw data. In general, LiDAR point cloud reflectance provides crucial cues for identifying 3D objects, thus improving the reliability of 3D object detection. In SparseKD-PV, the decision to discard reflectance information to enhance transmission efficiency is a key factor contributing to the suboptimal performance. While methods like Unicorn [7] reconstruct reflectance via a residual-based attribute bitstream using a DNN network, and PCC-S [9] does not transmit the attribute bitstream but needs alternative strategies to recover reflectance, we argue that relying solely on non-reflectance compressed point clouds

for detection misses important reflectance features. To address this limitation, we propose a dedicated reflectance prediction (RP) module at the receiver, which utilizes the geometric information of compressed point clouds and reflectance priors from raw point clouds. Additionally, to further enhance the accuracy of reflectance prediction, we introduce response-based reflectance knowledge distillation (RKD), which effectively guides the RP module during learning process, improving detection performance while maintaining efficient data transmission.

Incorporating the previous analysis, we propose a 3D object detection framework with reflectance prediction-based knowledge distillation (RPKD) to improve detection accuracy for non-reflectance compressed point clouds, as depicted in Fig. 1(d). Since compressed and raw point clouds lack direct point-to-point correspondence, we design a reflectance cross-match (RCM) module to assign reflectance labels from raw point-cloud voxels to compressed points. To construct suitable knowledge for reflectance distillation, we introduce a comparable reflectance inter-match (RIM) module to generate

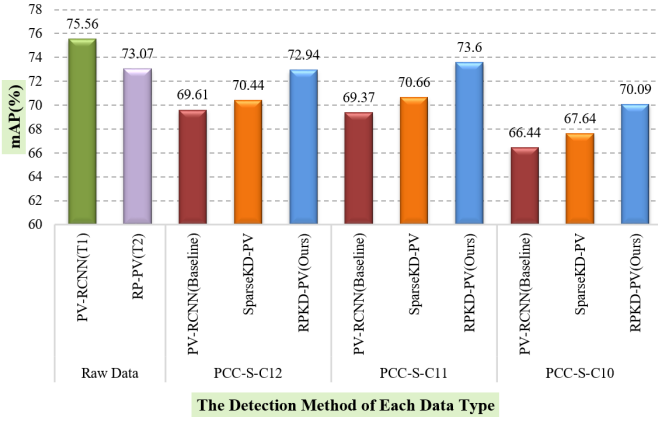


Fig. 2. Quantitative comparisons between raw and compressed data with PV-RCNN backbone on the KITTI validation split. T1 and T2 represent the teacher model of SparseKD-PV and our RPKD-PV, respectively. The detection methods and data types of this figure are detailed in Section IV-A.

reflectance labels for the raw point-cloud detector. Besides, the proposed reflectance prediction (RP) module comprehensively extracts geometric features of voxelized point clouds, achieving reflectance reconstruction at the receiver. Through our reflectance knowledge distillation (RKD) and detection knowledge distillation (DKD), rich teacher knowledge is transferred from raw to compressed point clouds for more precise reflectance reconstruction and robust 3D object detection. As shown in Fig. 2, RPKD-PV significantly increases the mAP values across multiple data types, which demonstrates the effectiveness of our RPKD framework for non-reflectance compressed point clouds.

In summary, the contributions of this work are as follows.

- We propose an RCM module to generate reflectance labels for compressed points based on the corresponding raw point-cloud voxels.
- At the receiver, we design a geometry-based RP module to reconstruct discarded reflectance, thereby improving detection performance for non-reflectance compressed point clouds.
- We introduce two response-based distillation constraints, namely RKD and DKD, to transfer supervisory knowledge from raw to compressed point-cloud detectors, further enhancing detection robustness for compressed point clouds.

The remainder of the paper is organized as follows. Section II reviews existing studies in terms of 3D object detection, point cloud compression, and knowledge distillation, highlighting relevant technologies. In Section III, we present the overall architecture of a 3D object detection framework with reflectance prediction-based knowledge distillation and elaborate on its key components. Section IV demonstrates the effectiveness of our method on the KITTI dataset and Waymo Open Dataset and includes ablation studies to evaluate the effect of each component. Finally, Section V concludes this paper.

II. RELATED WORK

A. 3D Object Detection

In 3D object detection for raw point clouds, existing methods can be sorted into two classes according to the data format of network input: point-based [14]–[21] and voxel-based [22]–[31] methods. Point-based detectors extract hierarchical point-wise features by various sampling and aggregation methods to predict 3D objects. In contrast, voxel-based detectors utilize 3D sparse convolution to extract voxel features, and these features are projected onto the Bird’s Eye View (BEV) for 3D object detection. In 3D object detection for compressed point clouds, those generated by range image-based [32]–[35] and voxel-based [8], [9] compression frameworks are input into compressed point-cloud detectors for recognition and localization. These methods generally rely on raw point clouds for pre-training 3D detectors and assess detection performance on lossy compressed point clouds across various code rates using the pre-trained models, as shown in Fig. 1(a) and 1(b). However, they lack effective robustness measures against information loss and reconstruction errors caused by lossy point cloud compression, leading to a significant decline in detection accuracy.

For robust 3D object detection in compressed point clouds, this paper addresses three key aspects. First, voxelized representation of compressed point clouds helps mitigate the negative effects of lossy compression. Thus, we develop robust compressed point-cloud detectors on voxel-based detection frameworks. Second, pre-training 3D detectors solely on raw point clouds is insufficient for adapting to the characteristics of compressed point clouds. To improve detection performance, our 3D detectors are trained on both raw and compressed point clouds. Finally, with a two-source joint training scheme, we use voxel-based two-stage detectors like PV-RCNN [22] and Voxel-RCNN [23] as backbone networks and transfer detection knowledge of the first-stage proposals from raw to compressed point-cloud detectors, thereby enhancing detection robustness for compressed point clouds.

B. Point Cloud Compression

LiDAR point cloud compression methods can be categorized into three classes based on data representation: point-based [36]–[38], image-based [32]–[35], [39]–[43], and voxel-based [5]–[13], [44] methods. Point-based methods utilize flexible point sampling and feature extraction to generate point-wise features, achieving point cloud compression and reconstruction. However, these methods are confronted with uneven 3D object loss and noise-point interference due to the lack of spatial structure and context information during lossy compression. Image-based methods project point clouds onto 2D images for quantization and encoding, but they introduce more severe three-dimensional spatial distortion and information loss compared to voxel-based methods. By analyzing octree or multi-scale sparse tensors, voxel-based methods enhance compression performance via context feature learning, multi-scale joint optimization, and redundant encoding reduction. Among these compression methods, only G-PCC [5] and Unicorn [7] incorporate reflectance encoding modules, as reflectance encoding presents challenges

in structural design, end-to-end optimization, and data-flow overhead. To solve this problem, we design an RP module at the receiver to supplement reflectance information for detection training on non-reflectance compressed point clouds generated by voxel-based methods. Our approach effectively alleviates the design complexity of LiDAR point cloud compression and provides an end-to-end optimization strategy for reflectance prediction at the receiver.

C. Knowledge Distillation

Knowledge distillation methods for 3D object detection can be divided into three categories according to their research objectives: model compression distillation [45]–[50], detection improvement distillation [51], [52], and weak-data robustness distillation [53]–[55]. In model compression distillation, SparseKD [45] introduces response-based constraints using Logit and Label KD to guide lightweight student models, achieving accurate and efficient 3D object detection. In detection improvement distillation, SPNet [51] assigns category values to the interior points of ground truth (GT) boxes, while X-Ray [52] addresses object point loss caused by sparsity and occlusion utilizing tracking information from consecutive-frame point clouds. Both methods augment data representations with strong semantic priors, providing valuable supervisory knowledge for distillation. In weak-data robustness distillation, student models employ low-quality point clouds from rainy conditions [55] or low-resolution sensor data [53], [54], learning complete and accurate knowledge from raw point clouds to improve detection robustness in weak data scenarios. Inspired

by these weak-data robustness distillation methods, our RPKD framework treats non-reflectance compressed point clouds involved in vehicle networking data transmission as weak data for student models and raw point clouds as guiding data for teacher models, aiming to develop robust compressed point-cloud detectors.

III. PROPOSED APPROACH

A. Overview of our Framework

During point cloud compression, reflectance encoding faces significant challenges in both end-to-end optimization and data-flow overhead. According to the separable compression mechanism of G-PCC [5], existing methods typically disregard reflectance compression and focus solely on optimizing geometric coordinate encoding to achieve efficient transmission and accurate detection. As a result, decoded compressed point clouds often lack reflectance information and suffer from point number reduction and reconstruction errors, which limit 3D object detection performance. To address this issue, we propose a 3D object detection framework with reflectance prediction-based knowledge distillation (RPKD), as shown in Fig. 3, to obtain more robust and precise 3D detectors against non-reflectance compressed point clouds.

First, our reflectance cross-match (RCM) module correlates lossy compressed points with neighboring raw point-cloud voxels. The nearest voxel’s average reflectance is assigned as the reflectance label for the current compressed point. Similarly, the reflectance inter-match (RIM) module assigns a voxel’s average reflectance as the reflectance label for corresponding

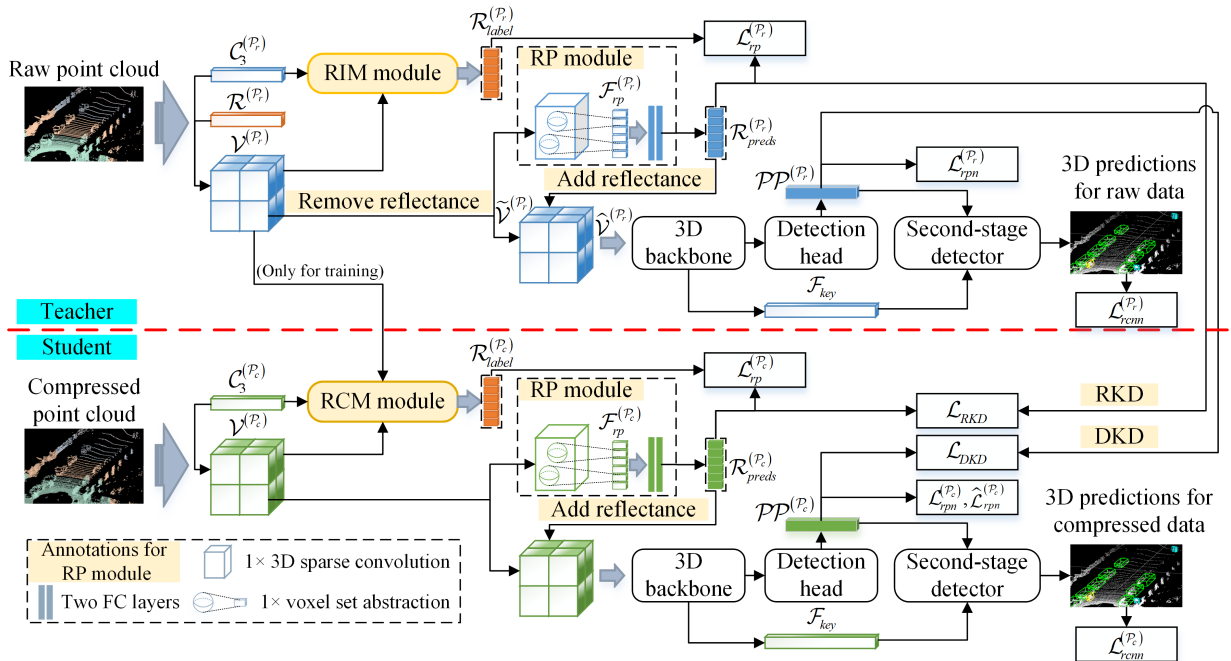


Fig. 3. Overview of our method. During student detector training, the RCM module assigns reflectance labels from raw point-cloud voxels to compressed points, while the RP module extracts geometric features to predict compressed point reflectance. In contrast, the teacher detector’s RP module predicts raw point reflectance based on labels obtained from the RIM module. The predicted reflectance is then incorporated into non-reflectance voxels for detection learning. With raw point clouds as teacher data, RKD transfers precise reflectance prediction knowledge, while DKD utilizes first-stage proposals to convey accurate detection knowledge.

raw points. Next, the proposed reflectance prediction (RP) module generates point-wise geometric features using 3D sparse convolution and voxel set extraction to predict reflectance. The predicted point-wise reflectance is then incorporated into corresponding non-reflectance voxels for subsequent detection tasks. Finally, we treat non-reflectance compressed point clouds as weak data and introduce two response-based knowledge distillation constraints: reflectance knowledge distillation (RKD) and detection knowledge distillation (DKD). Specifically, RKD transfers reflectance prediction knowledge from raw point clouds via the RP module, while DKD conveys first-stage proposal knowledge from the two-stage 3D detector for raw point clouds. In what follows, we detail the proposed framework.

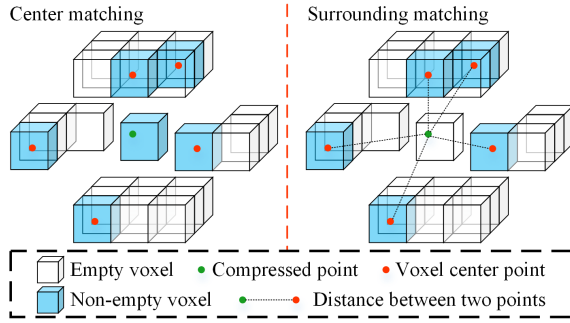


Fig. 4. Two matching methods of the RCM module. All voxels originate from voxelizing raw point clouds. If a compressed point lies within a non-empty voxel, the voxel’s mean reflectance is assigned to it. Otherwise, we search for the surrounding non-empty voxels within a 1-voxel matching range and use the nearest voxel’s mean reflectance as the matching value for this compressed point.

B. Reflectance Label Generation

Due to point number reduction and reconstruction errors from lossy compression, compressed points do not correspond one-to-one with raw points. For compressed point reflectance prediction, we introduce an RCM module based on spatial relationships to assign reflectance labels from raw point-cloud voxels to corresponding compressed points. These labels, used as prior knowledge for reflectance prediction, are generated frame by frame during detection training and do not need to be compressed or transmitted. Additionally, to transfer effective knowledge during reflectance distillation, we also design a similar RIM module to acquire reflectance labels for raw points. The principles of these modules are outlined below.

Reflectance Cross-match Module. For geometric coordinate encoding, voxel-based compression methods [6], [9] are often employed to obtain non-reflectance compressed point clouds $\widehat{\mathcal{P}}_c = \{c_{ci} | c_{ci} = (x_{ci}, y_{ci}, z_{ci}) \in \mathcal{C}_3^{(\mathcal{P}_c)}, i \in \{1, \dots, n_c\}\}$. Before training, with each point’s reflectance assigned to 0, the compressed point clouds fed into our detection networks are $\mathcal{P}_c = \{(c_{ci}, r_c) | c_{ci} = (x_{ci}, y_{ci}, z_{ci}) \in \mathcal{C}_3^{(\mathcal{P}_c)}, r_c = 0, i \in \{1, \dots, n_c\}\}$. Raw point clouds are represented as $\mathcal{P}_r = \{(c_{rk}, r_{rk}) | c_{rk} = (x_{rk}, y_{rk}, z_{rk}) \in \mathcal{C}_3^{(\mathcal{P}_r)}, r_{rk} \in \mathcal{R}^{(\mathcal{P}_r)}, k \in \{1, \dots, n_r\}\}$. These point clouds are voxelized to the same scale, generating compressed point-cloud voxels

$\mathcal{V}^{(\mathcal{P}_c)} = \{v_{cj} | j \in \{1, \dots, n_{vc}\}\}$ and raw point-cloud voxels $\mathcal{V}^{(\mathcal{P}_r)} = \{v_{rl} | l \in \{1, \dots, n_{vr}\}\}$. When using $\mathcal{C}_3^{(\mathcal{P}_c)}$, $\mathcal{V}^{(\mathcal{P}_c)}$ and $\mathcal{V}^{(\mathcal{P}_r)}$ as inputs, the principle of our RCM module can be described as follows.

As depicted in Fig. 4, there are two spatial matching strategies between compressed points and raw point-cloud voxels: center matching and surrounding matching. Specifically, the voxel corresponding to compressed point coordinates c_{ci} is denoted as $v_{center}^{(c_{ci})}$, and the surrounding non-empty voxels within a 1-voxel matching range are $\mathcal{V}_s^{(c_{ci})} = \{v_{sl}^{(c_{ci})} | v_{sl}^{(c_{ci})} \in \mathcal{V}^{(\mathcal{P}_r)}, l \in \{1, \dots, n_{vs}\}\}$. The initial reflectance labels for compressed points $\widehat{\mathcal{R}}_{label}^{(\mathcal{P}_c)}$ are defined as:

$$\widehat{\mathcal{R}}_{label}^{(\mathcal{P}_c)} = \begin{cases} r_m(v_{center}^{(c_{ci})}), & v_{center}^{(c_{ci})} \in \mathcal{V}^{(\mathcal{P}_r)}, \\ r_m(\arg \min d(c_{ci}, \mathcal{V}_s^{(c_{ci})})), & v_{center}^{(c_{ci})} \notin \mathcal{V}^{(\mathcal{P}_r)}, \end{cases} \quad (1)$$

where $r_m(v_{center}^{(c_{ci})})$ represents the average reflectance of $v_{center}^{(c_{ci})}$ in center matching, and $r_m(\arg \min d(c_{ci}, \mathcal{V}_s^{(c_{ci})}))$ is the nearest voxel’s average reflectance in surrounding matching. However, when multiple compressed points exist within the same compressed point-cloud voxel v_{cj} , their reflectance labels may come from different raw point-cloud voxels, resulting in significant numerical discrepancies that negatively impact compressed point reflectance prediction. To address this issue, we further calculate the average reflectance labels for all points within each compressed point-cloud voxel v_{cj} . The final reflectance labels for compressed points $\mathcal{R}_{label}^{(\mathcal{P}_c)}$ are thus expressed as:

$$\mathcal{R}_{label}^{(\mathcal{P}_c)} = \left[\mathcal{M}_c(\widehat{\mathcal{R}}_{label}^{(c_{ci})}, c_{ci}, v_{cj}) \Big| \widehat{\mathcal{R}}_{label}^{(c_{ci})} \in \widehat{\mathcal{R}}_{label}^{(\mathcal{P}_c)}, i \in \{1, \dots, n_c\}, j \in \{1, \dots, n_{vc}\} \right], \quad (2)$$

where $\widehat{\mathcal{R}}_{label}^{(c_{ci})}$ denotes the reflectance label for each point within the current compressed point-cloud voxel v_{cj} , and $\mathcal{M}_c(\cdot)$ represents the averaging operation applied to these reflectance labels.

Reflectance Inner-match Module. In the RPKD framework, it is crucial to establish suitable reflectance prediction knowledge from raw point clouds to guide the prediction process for compressed point-cloud reflectance. Specifically, we treat the reflectance predictions for compressed and raw point clouds as a student-teacher pair, where both sets of labels need to maintain spatial correspondence and information similarity. In the RCM module, the reflectance labels for compressed points are derived from the corresponding raw point-cloud voxels. Therefore, our RIM module avoids directly using raw point reflectance and instead assigns the average reflectance of raw point-cloud voxels to corresponding points as their reflectance labels. Since raw points exactly correspond to their voxels, our RIM module employs center matching. With raw point coordinates $\mathcal{C}_3^{(\mathcal{P}_r)}$ and voxels $\mathcal{V}^{(\mathcal{P}_r)}$ as inputs, the raw point reflectance labels $\mathcal{R}_{label}^{(\mathcal{P}_r)}$ are computed by the following formula:

$$\mathcal{R}_{label}^{(\mathcal{P}_r)} = \left[r_m(v_{center}^{(c_{rk})}) \Big| v_{center}^{(c_{rk})} \in \mathcal{V}^{(\mathcal{P}_r)}, k \in \{1, \dots, n_r\} \right], \quad (3)$$

where $v_{center}^{(c_{rk})}$ is the voxel corresponding to raw point coordinates c_{rk} , and $r_m(v_{center}^{(c_{rk})})$ denotes the average reflectance of this voxel.

C. Reflectance Prediction Module

Concerning the reflectance reconstruction of compressed point clouds, Unicorn [7] utilizes current-scale reflectance residual features and low-scale reflectance priors through a DNN module to predict reflectance. In contrast, our RP module exploits the geometric features of non-reflectance compressed point clouds and the reflectance priors of raw point clouds to achieve precise reflectance reconstruction at the receiver. This innovative design not only reduces the transmission rate in compression transmission systems but also enhances the robustness of 3D detectors against non-reflectance compressed point clouds. As shown in Fig. 3, the structure and principle of our RP module are detailed as follows.

RP Module for Compressed Point Clouds. In the compressed point-cloud detector, the RP module takes non-reflectance compressed point-cloud voxels $\mathcal{V}^{(\mathcal{P}_c)}$ as input. To accurately predict reflectance for compressed points, the RP module employs 3D sparse convolution to extract voxel features and voxel set extraction to refine point-wise features. We define the geometric features of compressed points $\mathcal{F}_{rp}^{(\mathcal{P}_c)}$ as:

$$\mathcal{F}_{rp}^{(\mathcal{P}_c)} = \mathcal{VSA}^{(1 \times)}(c_{ci}, \text{SConv}^{(1 \times)}(\mathcal{T}(\mathcal{V}^{(\mathcal{P}_c)}))), \quad (4)$$

$$i \in \{1, \dots, n_c\},$$

where $\mathcal{T}(\cdot)$ denotes a sparse tensor transformation module, $\text{SConv}(\cdot)^{(1 \times)}$ is the 3D sparse convolution with a $1 \times$ downsampling size (i.e., the initial size) in the voxel-wise basic backbone, and $\mathcal{VSA}(\cdot)^{(1 \times)}$ represents the $1 \times$ voxel set extraction corresponding to $\text{SConv}(\cdot)^{(1 \times)}$. The voxel set extraction structure in our RP module is identical to that in PV-RCNN [22], but the number of sampling points is equal to the number of compressed points in the current frame. Since the reflectance is a single-channel floating-point scalar in the range of $[0, 1]$, we use two fully connected (FC) layers as a prediction head to generate compressed point reflectance, denoted as $\mathcal{R}_{preds}^{(\mathcal{P}_c)} = \{r_{preds}^{(c_{ci})} | i \in \{1, \dots, n_c\}\}$. The predicted reflectance of compressed points, $\mathcal{R}_{preds}^{(\mathcal{P}_c)}$, is then incorporated into the corresponding compressed point-cloud voxels based on their spatial relationship for subsequent training and detection.

We screen the compressed point reflectance labels with values greater than zero, and define their indices as $I_c = \{i | r_{label}^{(c_{ci})} > 0, r_{label}^{(c_{ci})} \in \mathcal{R}_{label}^{(\mathcal{P}_c)}, i \in \{1, \dots, n_c\}\}$. We apply Mean Squared Error Loss (MSELoss) to constrain compressed point reflectance prediction, and the corresponding loss function $\mathcal{L}_{rp}^{(\mathcal{P}_c)}$ is expressed as follows:

$$\mathcal{L}_{rp}^{(\mathcal{P}_c)} = \frac{1}{|I_c|} \sum_{i \in I_c} (r_{preds}^{(c_{ci})} - r_{label}^{(c_{ci})})^2, \quad i \in \{1, \dots, n_c\}, \quad (5)$$

where $|I_c|$ represents the number of compressed point reflectance labels with values greater than zero.

RP Module for Raw Point Clouds. In 3D object detection knowledge distillation, maintaining similar network structures

between teacher and student detectors benefits the efficient transfer of teacher knowledge. Therefore, in this study, we design an analogous RP module in the raw point-cloud detector to predict raw point reflectance. Non-reflectance raw point-cloud voxels $\tilde{\mathcal{V}}^{(\mathcal{P}_r)}$ are fed into this module, and the geometric features of raw points $\mathcal{F}_{rp}^{(\mathcal{P}_r)}$ are represented as:

$$\mathcal{F}_{rp}^{(\mathcal{P}_r)} = \mathcal{VSA}^{(1 \times)}(c_{rk}, \text{SConv}^{(1 \times)}(\mathcal{T}(\tilde{\mathcal{V}}^{(\mathcal{P}_r)}))), \quad (6)$$

$$k \in \{1, \dots, n_r\}.$$

Subsequently, we predict raw point reflectance $\mathcal{R}_{preds}^{(\mathcal{P}_r)} = \{r_{preds}^{(c_{rk})} | k \in \{1, \dots, n_r\}\}$ and incorporate it into corresponding voxels to obtain raw point-cloud voxels with the recovered reflectance $\hat{\mathcal{V}}^{(\mathcal{P}_r)}$.

We screen the raw point reflectance labels that are greater than zero and define their indices as $I_r = \{k | r_{label}^{(c_{rk})} > 0, r_{label}^{(c_{rk})} \in \mathcal{R}_{label}^{(\mathcal{P}_r)}, k \in \{1, \dots, n_r\}\}$. The loss function for raw point reflectance prediction $\mathcal{L}_{rp}^{(\mathcal{P}_r)}$ is defined as:

$$\mathcal{L}_{rp}^{(\mathcal{P}_r)} = \frac{1}{|I_r|} \sum_{k \in I_r} (r_{preds}^{(c_{rk})} - r_{label}^{(c_{rk})})^2, \quad k \in \{1, \dots, n_r\}, \quad (7)$$

where $|I_r|$ represents the number of raw point reflectance labels with values greater than zero.

D. Reflectance Prediction-based Knowledge Distillation

In lossy compression, non-reflectance compressed point clouds undergo point number reduction and reconstruction errors, leading to incomplete and biased geometric information. If only these compressed point clouds are used for reflectance prediction and object detection, it is difficult to match the detection accuracy of raw point clouds. Drawing from the weak-data robustness research [53]–[55] in 3D object detection knowledge distillation, we treat the non-reflectance compressed point clouds as weak students, enabling them to learn accurate and complete knowledge from raw point clouds to improve detection performance for compressed point clouds. Specifically, we propose two components: RKD, which transfers reflectance prediction knowledge from our RP module, and DKD, which refines the first-stage proposals in the two-stage 3D object detector, as depicted in Fig. 3. Both proposed distillation methods fall under the response-based knowledge distillation category, and their principles are outlined as follows.

Reflectance Knowledge Distillation. Building upon the RP module's prediction outputs, we obtain the compressed point reflectance $\mathcal{R}_{preds}^{(\mathcal{P}_c)}$ and raw point reflectance $\mathcal{R}_{preds}^{(\mathcal{P}_r)}$. Since they do not have a one-to-one correspondence, we map the recovered teacher reflectance from raw point-cloud voxels $\hat{\mathcal{V}}^{(\mathcal{P}_r)}$ to corresponding compressed points. The mapped teacher reflectance of each compressed point serves as a soft label of RKD. According to the spatial relationship in the RCM module, the raw point-cloud voxel corresponding to compressed point coordinates c_{ci} is denoted as $\hat{v}_{rl}^{(c_{ci})}$, and the RKD soft labels \mathcal{R}_{RKD} are obtained by the following formula:

$$\mathcal{R}_{RKD} = [r_{RKD}(c_{ci}, \hat{v}_{rl}^{(c_{ci})}) | \hat{v}_{rl}^{(c_{ci})} \in \hat{\mathcal{V}}^{(\mathcal{P}_r)}], \quad (8)$$

$$i \in \{1, \dots, n_{RKD}\}, l \in \{1, \dots, n_{vr}\},$$

where $r_{RKD} \left(c_{ci}, \widehat{v}_{rl}^{(c_{ci})} \right)$ represents the mapped reflectance value from a raw point-cloud voxel $\widehat{v}_{rl}^{(c_{ci})}$ to corresponding compressed point coordinates c_{ci} , and n_{RKD} is the number of compressed points that can be successfully matched with raw point-cloud voxels in the RCM module. We also adopt MSELoss as the loss function to constrain the reflectance distillation process, and the RKD loss function \mathcal{L}_{RKD} is formulated as

$$\mathcal{L}_{RKD} = \frac{1}{n_{fg}^{(P_c)}} \sum_{i=1}^{n_{RKD}} \mathcal{F}\mathcal{G} \left(\left(r_{preds}^{(c_{ci})} - r_{RKD}^{(c_{ci})} \right)^2 \right), \quad (9)$$

$$r_{preds}^{(c_{ci})} \in \mathcal{R}_{preds}^{(P_c)}, r_{RKD}^{(c_{ci})} \in \mathcal{R}_{RKD}, i \in \{1, \dots, n_{RKD}\},$$

where $\mathcal{F}\mathcal{G}(\cdot)$ denotes screening foreground compression points during loss computation, and $n_{fg}^{(P_c)}$ is the number of foreground compression points.

Detection Knowledge Distillation. In Fig. 3, the two-stage 3D detector transfers key features \mathcal{F}_{key} from the first-stage network to the second-stage detector for detection refinement. Additionally, the first-stage dense proposals passed to the second stage inherently carry valuable detection knowledge for distillation. DKD combines the compressed point-cloud proposals $\mathcal{P}\mathcal{P}^{(P_c)} = \{p_{cls}^{(P_c)}, b_{box}^{(P_c)}\}$ and raw point-cloud proposals $\mathcal{P}\mathcal{P}^{(P_r)} = \{p_{cls}^{(P_r)}, b_{box}^{(P_r)}\}$ to form a student-teacher pair for response-based knowledge distillation. In these proposals, p_{cls} and b_{box} represent the sigmoid-activated classification scores and bounding boxes, respectively. For distillation constraints, we apply Logit KD proposed in SparseKD [45] to design the distillation loss. Therefore, the DKD loss function \mathcal{L}_{DKD} can be expressed as:

$$\mathcal{L}_{DKD} = \alpha_1 \mathcal{L}_{cls}^{KD} + \alpha_2 \mathcal{L}_{box}^{KD},$$

$$\mathcal{L}_{cls}^{KD} = \frac{1}{n_{fg}} \sum_{i=1}^{n_{fg}} \mathcal{L}_{MSE}^{(i)} \left(p_{cls}^{(P_c)}, p_{cls}^{(P_r)} \right), \quad (10)$$

$$\mathcal{L}_{box}^{KD} = \frac{1}{n_{fg}} \sum_{i=1}^{n_{fg}} \mathcal{L}_{SL}^{(i)} \left(b_{box}^{(P_c)}, b_{box}^{(P_r)} \right),$$

where $\mathcal{L}_{MSE}^{(i)}$ refers to the MSELoss of classification scores p_{cls} , $\mathcal{L}_{SL}^{(i)}$ represents the Smooth-L1 loss of bounding boxes b_{box} , and n_{fg} is the number of foreground objects in the first-stage proposals.

E. Loss Function

In this study, we pre-train separate detectors for the compressed and raw point clouds and initialize the training parameters of our RPKD framework using these pre-trained models. Therefore, the compressed point-cloud detection loss $\mathcal{L}^{(P_c)}$ and the raw point-cloud detection loss $\mathcal{L}^{(P_r)}$ are defined as follows:

$$\mathcal{L}^{(P_c)} = \lambda_1 \mathcal{L}_{rp}^{(P_c)} + \mathcal{L}_{rpn}^{(P_c)} + \mathcal{L}_{rcnn}^{(P_c)}, \quad (11)$$

$$\mathcal{L}_{rpn}^{(P_c)} = \beta_1 \mathcal{L}_{cls}^{(P_c)} + \beta_2 \mathcal{L}_{box}^{(P_c)} + \beta_3 \mathcal{L}_{dir}^{(P_c)},$$

$$\mathcal{L}^{(P_r)} = \lambda_1 \mathcal{L}_{rp}^{(P_r)} + \mathcal{L}_{rpn}^{(P_r)} + \mathcal{L}_{rcnn}^{(P_r)}, \quad (12)$$

$$\mathcal{L}_{rpn}^{(P_r)} = \beta_1 \mathcal{L}_{cls}^{(P_r)} + \beta_2 \mathcal{L}_{box}^{(P_r)} + \beta_3 \mathcal{L}_{dir}^{(P_r)},$$

where \mathcal{L}_{rp} , \mathcal{L}_{cls} , \mathcal{L}_{box} and \mathcal{L}_{dir} represent the reflectance prediction, classification, bounding box and orientation losses of the first-stage detector, respectively. The corresponding weight

coefficients are λ_1 , β_1 , β_2 and β_3 . \mathcal{L}_{rcnn} denotes the second-stage detector loss with a weight coefficient of 1. On this basis, the overall loss function of our RPKD framework \mathcal{L}_{RPKD} is formulated as follows:

$$\mathcal{L}_{RPKD} = \lambda_1 \mathcal{L}_{rp}^{(P_c)} + \widehat{\mathcal{L}}_{rpn}^{(P_c)} + \mathcal{L}_{rcnn}^{(P_c)} + \lambda_2 \mathcal{L}_{RKD} + \lambda_3 \mathcal{L}_{DKD},$$

$$\widehat{\mathcal{L}}_{rpn}^{(P_c)} = \beta_1 \widehat{\mathcal{L}}_{cls}^{(P_c)} + \beta_2 \widehat{\mathcal{L}}_{box}^{(P_c)} + \beta_3 \widehat{\mathcal{L}}_{dir}^{(P_c)}, \quad (13)$$

where $\widehat{\mathcal{L}}_{cls}^{(P_c)}$, $\widehat{\mathcal{L}}_{box}^{(P_c)}$ and $\widehat{\mathcal{L}}_{dir}^{(P_c)}$ are the classification, bounding box and orientation losses of the first-stage detector based on Label KD in SparseKD [45]. The weight coefficients for the distillation losses are λ_2 and λ_3 .

IV. EXPERIMENTS

For 3D object detection in compressed point clouds, we utilized LiDAR point clouds from the KITTI dataset and Waymo Open Dataset (WOD) as raw point-cloud inputs for the compression network. Subsequently, we compressed and reconstructed the geometric coordinates of these point clouds at multiple code rates through deep learning-based PCC-S, resulting in non-reflectance compressed point clouds. The proposed RPKD framework was trained on both compressed and raw point clouds, using only compressed point clouds for inference. Extensive experiments demonstrate that our method significantly enhances detection robustness for non-reflectance compressed point clouds generated by voxel-based compression. The following sections provide a comprehensive explanation of the implementation details, result comparisons, and ablation analysis.

A. Implementation Details

1) *Datasets and Hardware:* For the KITTI dataset, we used 7481 labeled training samples as raw point clouds, dividing them into a training split with 3712 samples and a validation split with 3769 samples. Firstly, the PCC-S network employed the training split of raw point clouds for compression learning and reconstructed 7481 frames of point clouds through the trained compression model at octree levels of 12, 11, and 10, respectively. Regarding the training configuration, we trained the PCC-S network for 20 epochs on a single RTX 8000 GPU with a batch size of 2 and a maximum octree level of 12. Then, we established independent models for each code rate and conducted joint training on both the compressed and raw point clouds to build robust 3D detectors for compressed point clouds. These detectors were trained for 80 epochs on 4 RTX 4090 GPUs with a batch size of 16.

WOD is a large-scale detection dataset composed of 798 training sequences and 202 validation sequences. Due to the limited training efficiency of PCC-S and the computing power of a single RTX 8000 GPU, we only selected 20 training sequences and 10 validation sequences for research. Thus, the raw point clouds consisted of a training split with 3966 samples and a validation split with 1967 samples. Using the same training configuration as KITTI, we obtained 5933 frames of compressed point clouds by PCC-S on WOD at octree levels 12, 11, and 10, respectively. Additionally, the detectors of our RPKD framework were trained for 30 epochs on 4 RTX 4090 GPUs with a batch size of 8.

TABLE I

THE 3D OBJECT DETECTION PERFORMANCE ON THE KITTI VALIDATION SPLIT, WHICH INCLUDES AP AND MAP WITH 40 RECALL POSITIONS. BOLDDED VALUES ARE THE HIGHER PERFORMANCES WITHIN EACH COMPARISON PAIR. T2 AND T3 REPRESENT THE TEACHER MODEL OF OUR RPKD-PV AND RPKD-VOXEL, RESPECTIVELY.

Data Type	Method	Car 3D			Ped. 3D			Cyc. 3D			mAP
		Easy	Mod.	Hard	Easy	Mod.	Hard	Easy	Mod.	Hard	
Raw Data	PV-RCNN	91.97	84.72	82.32	68.60	60.61	55.55	92.06	74.48	69.63	75.56
	RP-PV(T2)	92.10	84.36	82.29	63.62	56.35	50.88	90.30	70.75	66.96	73.07
	Voxel-RCNN	92.55	84.65	82.41	66.07	59.30	53.73	92.81	73.55	68.97	74.89
	RP-Voxel(T3)	92.18	84.12	81.75	62.04	56.11	51.05	93.67	72.87	68.41	73.58
PCC-S-C12 (Bpp=3.864)	PV-RCNN(Baseline)	91.48	82.51	80.72	56.17	49.66	45.37	87.85	68.51	64.21	69.61
	RPKD-PV(Ours)	92.02	83.13	80.21	65.72	58.68	53.72	90.39	68.63	63.92	72.94
	Voxel-RCNN(Baseline)	92.27	82.79	80.17	63.64	56.21	51.21	90.69	71.35	66.92	72.81
	RPKD-Voxel(Ours)	92.06	82.91	79.98	70.40	64.14	57.63	92.26	70.31	65.84	75.06
PCC-S-C11 (Bpp=2.146)	PV-RCNN(Baseline)	90.85	82.25	80.33	57.79	50.83	46.20	88.92	65.79	61.40	69.37
	RPKD-PV(Ours)	91.38	82.95	79.96	70.93	62.81	56.39	89.21	66.68	62.09	73.60
	Voxel-RCNN(Baseline)	92.03	82.72	80.16	61.49	54.77	49.30	88.27	67.99	63.97	71.19
	RPKD-Voxel(Ours)	91.78	83.00	80.30	70.33	63.36	57.17	92.12	68.10	63.54	74.41
PCC-S-C10 (Bpp=1.047)	PV-RCNN(Baseline)	90.74	81.40	79.24	54.71	47.58	44.12	81.08	61.64	57.45	66.44
	RPKD-PV(Ours)	91.53	82.52	79.45	63.24	57.24	51.90	85.51	61.70	57.68	70.09
	Voxel-RCNN(Baseline)	90.96	81.37	78.73	60.10	51.66	45.88	83.05	62.86	58.62	68.14
	RPKD-Voxel(Ours)	90.67	81.87	78.95	65.95	59.02	53.54	87.79	64.80	60.35	71.44

2) *Training Parameters*: In the RCM module, we matched compressed points with raw point-cloud voxels within a 1-voxel matching range, corresponding to $3 \times 3 \times 3$ spatial voxels. During pre-training, the compressed and raw point-cloud detectors shared the same loss weights, and these loss weights $(\lambda_1, \beta_1, \beta_2, \beta_3)$ were set to $(3, 1, 2, 0.2)$. In the knowledge distillation stage, we designed two distillation methods, RKD and DKD, whose loss weights (λ_2, λ_3) were set to $(10, 1)$. Specifically, the distillation constraints for DKD consisted of classification distillation loss \mathcal{L}_{cls}^{KD} and bounding box distillation loss \mathcal{L}_{box}^{KD} , and their loss weights (α_1, α_2) were $(6, 0.5)$. For dataset configuration, we trained compressed point-cloud detectors using the standard parameters of public datasets and expanded single-source data to two-source data for joint processing.

3) *Evaluation Metrics*: We evaluated the robustness of our RPKD framework for 3D object detection on compressed point clouds using the KITTI and WOD validation splits. The primary metric for KITTI was average precision (AP) at 40 recall positions with 3D IoU thresholds of 0.7, 0.5, and 0.5 for cars, pedestrians, and cyclists, respectively. For WOD, the metrics were AP and average precision weighted by heading (APH). To compare performance across multiple code rates and methods, we used mean Average Precision (mAP) and mean APH (mAPH) across categories and difficulty levels. The Bit-per-point (Bpp) metric represents the average number of bits required to encode each point, indicating the code rate of compressed point clouds.

4) *Controlled Experiment Design*: Firstly, in terms of data types, raw data, PCC-S-C12, PCC-S-C11, and PCC-S-C10 represented raw point clouds, the compressed point clouds of octree levels 12, 11, and 10, respectively. Then, the detection performance of PV-RCNN at each code rate served as the baseline, and the designed control experiments involved three detection methods, namely SparseKD-PV, RPV-KD, and RPKD-PV. In SparseKD-PV, with the teacher detector of PV-RCNN (T1) on raw data, we utilized Logit KD and Label KD for

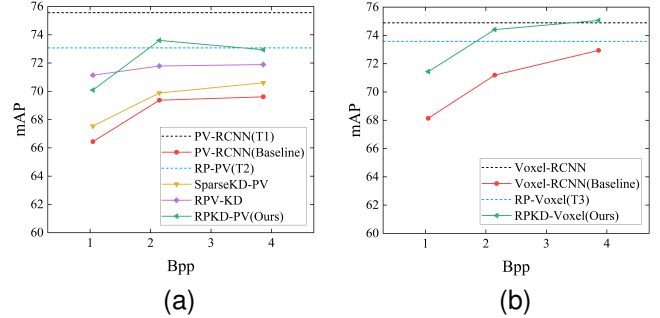


Fig. 5. Quantitative results of 3D object detection on the KITTI validation split. (a) Quantitative comparisons between a baseline, two teacher models and three student models across diverse KD frameworks, where all methods are based on the PV-RCNN backbone. (b) Generalization verification of our RPKD framework on the Voxel-RCNN backbone. T1, T2, and T3 denote the teacher model of SparseKD-PV, RPKD-PV (ours), and RPKD-Voxel (ours), respectively.

distillation learning and performance evaluation of compressed point-cloud detectors. RPV-KD and SparseKD-PV share the same teacher model and distillation methods, while the key difference is that RPV-KD mapped raw point reflectance into corresponding compressed points based on the matching principle of our RCM module (Section III-B) to simulate compressed point clouds with decoded reflectance. RPKD-PV denotes the implementation of our method on the PV-RCNN backbone, with RP-PV (T2) as the teacher detector. Finally, referring to the experimental settings of RPKD-PV, we performed generalization verification of our method on the Voxel-RCNN backbone with RPKD-Voxel, using RP-Voxel (T3) as the teacher detector.

B. Experimental Results

Table I presents the performance improvement of our RPKD framework in 3D object detection for compressed point clouds with the PV-RCNN and Voxel-RCNN backbones on the KITTI

TABLE II

THE 3D OBJECT DETECTION PERFORMANCE ON THE WOD VALIDATION SPLIT. WE REPORT THE AP/APH RESULTS OF VEHICLE AND PEDESTRIAN CLASSES. BOLDDED VALUES REPRESENT THE HIGHER PERFORMANCES WITHIN EACH COMPARISON PAIR. THE PERFORMANCE OF CYCLIST CLASS IS NOT SHOWN DUE TO THE FEW SAMPLES OF CYCLISTS IN THE TRAINING SPLIT. T2 REPRESENTS THE TEACHER MODEL OF OUR RPKD-PV.

Data Type	Detection Method	Vehicle(L1)	Vehicle(L2)	Pedestrian(L1)	Pedestrian(L2)	mAP/mAPH
Raw Data	PV-RCNN	61.37/60.01	53.20/52.00	65.69/33.70	59.00/30.27	59.82/43.99
	RP-PV(T2)	61.75/60.76	53.44/52.56	60.42/29.80	54.14/26.70	57.44/42.46
PCC-S-C12 (Bpp=4.637)	PV-RCNN(Baseline)	61.27/60.07	52.87/51.81	59.89/30.98	53.60/27.78	56.91/42.66
	RPKD-PV(Ours)	62.08/61.02	53.72/52.77	59.62/ 34.44	53.37/30.82	57.20/44.76
PCC-S-C11 (Bpp=2.711)	PV-RCNN(Baseline)	60.51/59.52	52.30/51.43	58.75/29.72	52.57/26.61	56.03/41.82
	RPKD-PV(Ours)	61.41/60.38	53.22/52.30	58.33/ 32.55	52.21/29.14	56.29/43.59
PCC-S-C10 (Bpp=1.359)	PV-RCNN(Baseline)	60.09/58.81	51.95/50.82	56.76/26.30	50.77/23.53	54.89/39.86
	RPKD-PV(Ours)	61.13/60.04	52.92/51.95	57.49/28.16	51.45/25.20	55.75/41.34

TABLE III

THE 3D DETECTION PERFORMANCE OF DIFFERENT RP MODULE SETTINGS ON THE KITTI VALIDATION SPLIT OF PCC-S-C11. THE ABOVE RESULTS ARE ACQUIRED BY TRAINING ON THE 15% TRAINING SPLIT OF PCC-S-C11. THE BOLDDED VALUE REPRESENTS THE HIGHEST PERFORMANCE.

λ_1		[Ks, Pd, (Rd1, Rd2)]		Layer Quantity		mAP
1	3	[3, 1, (0.4, 0.8)]	[5, 2, (0.8, 1.2)]	1×	(1×, 2×)	
×	×	×	✓	✓	×	61.31
×	✓	✓	×	×	✓	61.81
✓	×	✓	×	✓	×	62.59
×	✓	✓	×	✓	×	63.70

validation split. For the compressed point clouds of PCC-S-C12, PCC-S-C11, and PCC-S-C10, RPKD-PV increases mAP by 3.33, 4.23, and 3.65, while RPKD-Voxel improves mAP by 2.25, 3.22, and 3.3. As a result, it reveals that the detectors of our RPKD framework exhibit consistent effectiveness and robustness across multiple code rates and backbones. Additionally, for compressed point clouds with the same code-rate order, RPKD-PV boosts the AP values for moderate-level pedestrians by 9.02, 11.98, and 9.66, respectively, and RPKD-Voxel elevates the AP values for moderate-level pedestrians by 7.93, 8.59, and 7.36. These findings highlight the significant enhancement in 3D detector robustness for challenging small-sized pedestrians within compressed point clouds.

As depicted in Fig. 5(a), based on the PV-RCNN backbone, we compare the detection performance of PV-RCNN (baseline), existing SparseKD, simulated RPV-KD and our RPKD on the KITTI compressed point clouds across multiple code rates. RPKD-PV achieves higher mAP values in both medium and high code rates, and its mAP value in the medium code rate exceeds that of RP-PV (T2). Fig. 5(b) shows the generalization performance of our RPKD framework on the Voxel-RCNN backbone. RPKD-Voxel outperforms Voxel-RCNN (baseline) in all code rates, and its mAP value surpasses that of RP-Voxel (T3) and Voxel-RCNN backbone in the high code rate. These results vividly illustrate the outstanding robustness and remarkable enhancement capabilities of our method in 3D object detection for compressed point clouds.

For the generalization ability in WOD, we evaluate the detection performance of our RPKD framework across multiple code rates with the PV-RCNN backbone on the validation split. In Table II, RPKD-PV improves mAP/mAPH for PCC-S-C12, PCC-S-C11, and PCC-S-C10 by 0.29/2.1, 0.26/1.77, and 0.86/1.48, respectively. For the compressed point clouds of PCC-S-C12, the APH values for vehicle and pedestrian cat-

TABLE IV

THE 3D DETECTION PERFORMANCE OF CRITICAL ELEMENTS FOR OUR RPKD FRAMEWORK ON THE KITTI VALIDATION SPLIT OF PCC-S-C11. THE BOLDDED VALUE REPRESENTS THE HIGHEST PERFORMANCE.

$\mathcal{M}_c(\cdot)$	Options of RKD			Detectors of DKD		mAP
	$\mathcal{F}_G(\cdot)$	Voxel-wise	Point-wise	PV-RCNN	RP-PV	
×	×	×	×	×	×	71.39
✓	×	×	×	×	×	72.00
×	✓	×	✓	×	×	69.12
✓	×	✓	×	×	×	70.16
✓	✓	✓	×	×	×	71.68
✓	✓	✓	×	✓	×	71.57
✓	✓	✓	×	×	✓	73.60

TABLE V

THE 3D DETECTION PERFORMANCE OF DESIGNED MODULES FOR OUR RPKD FRAMEWORK ON THE KITTI VALIDATION SPLIT OF PCC-S-C11. THE BOLDDED VALUE REPRESENTS THE HIGHEST PERFORMANCE.

RP Module	RKD	DKD	mAP
×	×	×	69.37
✓	×	×	72.00
✓	✓	×	71.68
✓	✓	✓	73.60

egories exceed those of RP-PV (T2) and PV-RCNN backbone on raw data. The experimental results demonstrate that our RPKD framework maintains consistent effectiveness throughout diverse code rates, backbone networks and detection datasets.

C. Ablation Study

We conducted comprehensive ablation experiments with the PV-RCNN backbone to verify the effectiveness of our RPKD framework. In this section, we used raw point clouds from the KITTI dataset and their corresponding compressed point clouds of PCC-S-C11 as experimental data. The evaluation metric is the mAP of compressed point-cloud detectors on the KITTI validation split.

1) *Different Configurations of RP Module:* For non-reflectance compressed point-cloud voxels, the RP module employed 3D sparse convolution and voxel set extraction to generate point-wise geometric features for compressed point reflectance prediction. In terms of expanding receptive field, we modified the kernel size (Ks) and padding (Pd) of 1× 3D sparse convolution, as well as the pooling radius (Rd1, Rd2) of 1× voxel set extraction. To assess the impact of network layer quantity on detection performance, we designed two

network schemes: a single-layer network $1\times$ and a double-layer network ($1\times, 2\times$). Additionally, we also adjusted the RP module’s loss weight for performance comparison. As shown in Table III, when using the single-layer network $1\times$ with $[K_s, P_d, (Rd1, Rd2)] = [3, 1, (0.4, 0.8)]$ and $\lambda_1 = 3$, the compressed point-cloud detector achieves optimal detection performance.

2) *Critical Elements of Our RPKD*: As indicated in Table IV, we assessed the influences of critical elements in our RPKD framework on the detection performance for compressed point clouds. In the first two rows, we compared the pre-training performance of compressed point-cloud detectors, where $\mathcal{M}_c(\cdot)$ refers to the voxel-based averaging operation in the RCM module. $\mathcal{FG}(\cdot)$ denotes screening foreground

compressed points in calculating reflectance distillation loss. In the third row, we used the matched raw point reflectance as the distillation label during point-wise RKD and did not perform the voxel-based $\mathcal{M}_c(\cdot)$. In contrast, we utilized the matched reflectance of raw point-cloud voxels as the distillation label during voxel-wise RKD and conducted the voxel-based $\mathcal{M}_c(\cdot)$, as shown in the fourth row. In Table IV, PV-RCNN and RP-PV represent raw point-cloud detector types that provided the first-stage proposals for DKD. As indicated in the last row, our RPKD framework achieves the best performance with these settings.

3) *Designed Modules of Our RPKD*: As shown in Table V, we evaluated the designed module’s effectiveness in 3D object detection for compressed point clouds. The first row

TABLE VI

THE 3D OBJECT DETECTION PERFORMANCE OF A UNIFIED MODEL ON THE KITTI VALIDATION SPLIT, WHICH INCLUDES AP AND MAP WITH 40 RECALL POSITIONS. BOLDDED VALUES ARE THE HIGHER PERFORMANCES WITHIN EACH COMPARISON PAIR. T2 REPRESENTS THE TEACHER MODEL OF RPKD-PV (UNIFIED).

Data Type	Method	Car 3D			Ped. 3D			Cyc. 3D			mAP
		Easy	Mod.	Hard	Easy	Mod.	Hard	Easy	Mod.	Hard	
Raw Data	PV-RCNN	91.97	84.72	82.32	68.60	60.61	55.55	92.06	74.48	69.63	75.56
	RP-PV(T2)	92.10	84.36	82.29	63.62	56.35	50.88	90.30	70.75	66.96	73.07
PCC-S-C12 (Bpp=3.864)	PV-RCNN(Baseline)	91.48	82.51	80.72	56.17	49.66	45.37	87.85	68.51	64.21	69.61
	RPKD-PV(Unified)	91.46	82.92	80.01	65.55	58.14	53.16	90.54	67.30	62.98	72.45
PCC-S-C11 (Bpp=2.146)	PV-RCNN(Baseline)	90.85	82.25	80.33	57.79	50.83	46.20	88.92	65.79	61.40	69.37
	RPKD-PV(Unified)	91.20	82.37	79.29	66.71	59.32	54.18	87.66	66.86	62.26	72.21
PCC-S-C10 (Bpp=1.047)	PV-RCNN(Baseline)	90.74	81.40	79.24	54.71	47.58	44.12	81.08	61.64	57.45	66.44
	RPKD-PV(Unified)	91.37	82.37	79.48	65.38	58.05	52.91	85.69	61.66	57.44	70.48

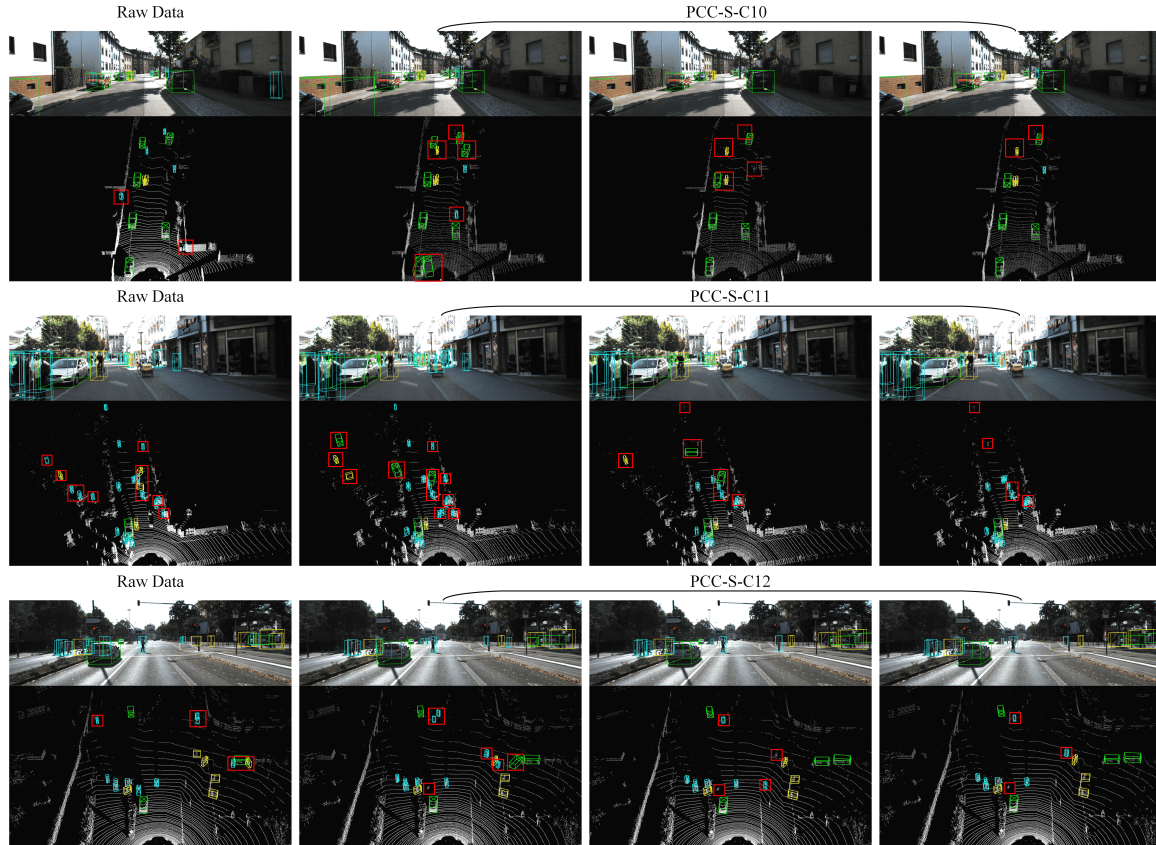


Fig. 6. Visual comparisons of different data types and detection methods on the KITTI validation split. The detection methods for the results in each column, from left to right, are: PV-RCNN, PV-RCNN (baseline), SparseKD-PV, and RPKD-PV. The false positives and missed detections are highlighted with red rectangles.

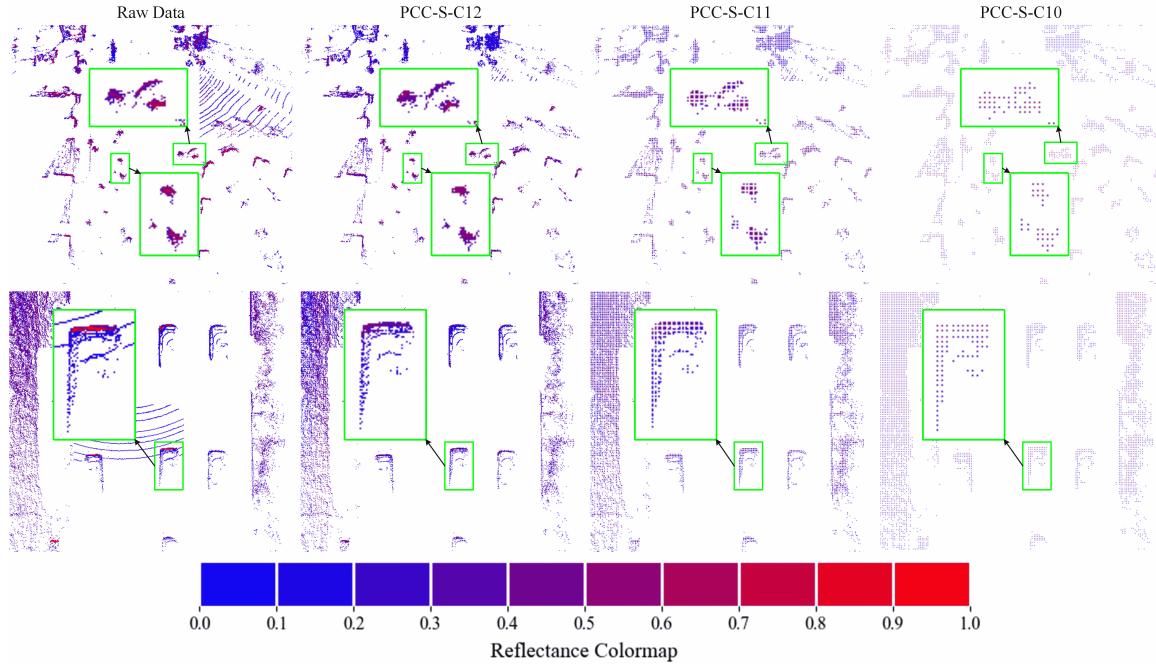


Fig. 7. Visual comparison of reflectance between raw data and compressed point clouds across various code rates in BEV. Raw data is directly colored based on its actual reflectance, while compressed point clouds are colored using reflectance prediction values from the RP module. Green rectangular boxes highlight and enlarge some foreground objects for better visibility.

displays the detection performance of PV-RCNN (baseline) for compressed point clouds of PCC-S-C11. We then incrementally introduced the RP module, RKD and DKD into the detector and reported corresponding mAP values. All the designed modules improve the performance of PV-RCNN (baseline), with the best mAP value achieved when all modules are utilized together.

4) *Experiments for a Unified Model*: To develop a unified detector applicable to various code rates, we combined the KITTI training splits of PCC-S-C10, PCC-S-C11, and PCC-S-C12 in a 1 : 1 : 1 ratio as input for the unified model. The trained model was then used to perform inference on each validation split of these compressed point clouds to evaluate detection performance. As shown in Table VI, RPKD-PV (unified) increases mAP by 2.84 for both PCC-S-C12 and PCC-S-C11, and by 4.04 for PCC-S-C10. These results demonstrate that our RPKD framework under a unified model achieves consistent effectiveness across diverse code rates.

5) *Visual Comparisons of Detection Results*: As depicted in Fig. 6, we performed visual comparisons of different data types and detection methods on the KITTI validation split. For compressed point-cloud detectors, RPKD-PV achieves fewer false positives and missed detections across multiple code rates, demonstrating the stronger robustness of our RPKD framework in 3D object detection for compressed point clouds. However, compared to the raw point-cloud detector based on PV-RCNN, RPKD-PV tends to miss objects with fewer points or at farther distances, which reveals a limitation of our method in detecting such challenging objects.

6) *Visual Comparisons of Reflectance Prediction*: In each BEV grid, we selected the maximum reflectance value from either raw data or compressed point clouds for coloring the corresponding visual points. As shown in Fig. 7, the predicted

reflectance in compressed point clouds closely matches the actual reflectance in raw data within the major reflective areas of foreground objects. These results demonstrate that our RP module accurately predicts the reflectance of foreground objects across various code rates, thereby improving detection robustness for compressed point clouds.

D. Discussion of Limitation and Future Work

For non-reflectance compressed point clouds, this paper effectively supplements the missing reflectance information through the RP module and RKD, thus enhancing detection robustness. However, as shown in Table I and Table II, the APs for pedestrians in WOD and for moderate-level cars and bicycles in KITTI still fall short of the corresponding APs achieved with raw point clouds. This may be because RPKD focuses on transferring detection knowledge via DKD without performing explicit geometric enhancement on lossy compressed point clouds. In future work, we plan to explore geometric enhancement modules at the receiver to recover missing spatial details, thereby further improving the robustness of 3D object detection against non-reflectance compressed point clouds.

V. CONCLUSION

We have presented a 3D object detection framework with reflectance prediction-based knowledge distillation (RPKD) to improve detection accuracy for non-reflectance compressed point clouds. During detection training, the designed RCM module assigns the average reflectance of raw point-cloud voxels to corresponding compressed points based on their

spatial relationship, providing essential prior labels for reflectance reconstruction. Treating non-reflectance compressed point clouds as weak students, the geometry-based RP module plays a critical role in precise reflectance prediction and object detection within compressed point-cloud detectors. The raw point-cloud detector, with the same structure, transfers the accurate reflectance prediction and object detection knowledge through RKD and DKD, significantly enhancing the robustness of compressed point-cloud detectors. Experimental results on the KITTI dataset and WOD demonstrate that our RPKD framework consistently improves detection performance for compressed point clouds across various code rates and backbone networks.

REFERENCES

- [1] Q. Chen, S. Tang, Q. Yang, and S. Fu, "Cooper: Cooperative perception for connected autonomous vehicles based on 3d point clouds," in *2019 IEEE 39th International Conference on Distributed Computing Systems (ICDCS)*. IEEE, 2019, pp. 514–524.
- [2] E. Ye, P. Spiegel, and M. Althoff, "Cooperative raw sensor data fusion for ground truth generation in autonomous driving," in *2020 IEEE 23rd International Conference on Intelligent Transportation Systems (ITSC)*. IEEE, 2020, pp. 1–7.
- [3] R. Xu, X. Xia, J. Li, H. Li, S. Zhang, Z. Tu, Z. Meng, H. Xiang, X. Dong, R. Song *et al.*, "V2v4real: A real-world large-scale dataset for vehicle-to-vehicle cooperative perception," in *Proceedings of the IEEE/CVF Conference on Computer Vision and Pattern Recognition*, 2023, pp. 13 712–13 722.
- [4] Z. Bai, G. Wu, M. J. Barth, Y. Liu, E. A. Sisbot, K. Oguchi, and Z. Huang, "A survey and framework of cooperative perception: From heterogeneous singleton to hierarchical cooperation," *IEEE Transactions on Intelligent Transportation Systems*, 2024.
- [5] C. Cao, M. Preda, V. Zakharchenko, E. S. Jang, and T. Zaharia, "Compression of sparse and dense dynamic point clouds—methods and standards," *Proceedings of the IEEE*, vol. 109, no. 9, pp. 1537–1558, 2021.
- [6] J. Wang, R. Xue, J. Li, D. Ding, Y. Lin, and Z. Ma, "A versatile point cloud compressor using universal multiscale conditional coding—part i: Geometry," *IEEE transactions on pattern analysis and machine intelligence*, vol. 47, no. 1, pp. 269–287, 2024.
- [7] J. Wang, R. Xue, J. Li, D. Ding, Y. Lin, and Z. Ma, "A versatile point cloud compressor using universal multiscale conditional coding—part ii: Attribute," *IEEE transactions on pattern analysis and machine intelligence*, vol. 47, no. 1, pp. 252–268, 2024.
- [8] Z. Que, G. Lu, and D. Xu, "Voxelcontext-net: An octree based framework for point cloud compression," in *Proceedings of the IEEE/CVF Conference on Computer Vision and Pattern Recognition*, 2021, pp. 6042–6051.
- [9] Z. Chen, Z. Qian, S. Wang, and Q. Chen, "Point cloud compression with sibling context and surface priors," in *European Conference on Computer Vision*. Springer, 2022, pp. 744–759.
- [10] C. Fu, G. Li, R. Song, W. Gao, and S. Liu, "Octattention: Octree-based large-scale contexts model for point cloud compression," in *Proceedings of the AAAI conference on artificial intelligence*, vol. 36, no. 1, 2022, pp. 625–633.
- [11] M. A. Lodhi, J. Pang, and D. Tian, "Sparse convolution based octree feature propagation for lidar point cloud compression," in *ICASSP 2023-2023 IEEE International Conference on Acoustics, Speech and Signal Processing (ICASSP)*. IEEE, 2023, pp. 1–5.
- [12] J. Wang, D. Ding, Z. Li, X. Feng, C. Cao, and Z. Ma, "Sparse tensor-based multiscale representation for point cloud geometry compression," *IEEE Transactions on Pattern Analysis and Machine Intelligence*, vol. 45, no. 7, pp. 9055–9071, 2022.
- [13] K. You, T. Chen, D. Ding, M. S. Asif, and Z. Ma, "Reno: Real-time neural compression for 3d lidar point clouds," *arXiv preprint arXiv:2503.12382*, 2025.
- [14] S. Shi, X. Wang, and H. Li, "Pointcnn: 3d object proposal generation and detection from point cloud," in *Proceedings of the IEEE/CVF conference on computer vision and pattern recognition*, 2019, pp. 770–779.
- [15] C. Chen, Z. Chen, J. Zhang, and D. Tao, "Sasa: Semantics-augmented set abstraction for point-based 3d object detection," in *Proceedings of the AAAI Conference on Artificial Intelligence*, vol. 36, no. 1, 2022, pp. 221–229.
- [16] Y. Zhang, Q. Hu, G. Xu, Y. Ma, J. Wan, and Y. Guo, "Not all points are equal: Learning highly efficient point-based detectors for 3d lidar point clouds," in *Proceedings of the IEEE/CVF conference on computer vision and pattern recognition*, 2022, pp. 18 953–18 962.
- [17] Y. Zhang, Q. Zhang, J. Hou, Y. Yuan, and G. Xing, "Unleash the potential of image branch for cross-modal 3d object detection," in *Advances in Neural Information Processing Systems*, vol. 36, 2023.
- [18] S. Dong, X. Kong, X. Pan, F. Tang, W. Li, Y. Chang, and W. Dong, "Semantic-context graph network for point-based 3d object detection," *IEEE Transactions on Circuits and Systems for Video Technology*, vol. 33, no. 11, pp. 6474–6486, 2023.
- [19] T. Xie, L. Wang, K. Wang, R. Li, X. Zhang, H. Zhang, L. Yang, H. Liu, and J. Li, "Farp-net: Local-global feature aggregation and relation-aware proposals for 3d object detection," *IEEE Transactions on Multimedia*, vol. 26, pp. 1027–1040, 2023.
- [20] X. He, Z. Wang, J. Lin, K. Nai, J. Yuan, and Z. Li, "Do-sa&r: Distant object augmented set abstraction and regression for point-based 3d object detection," *IEEE Transactions on Image Processing*, vol. 32, pp. 5852–5864, 2023.
- [21] M. Feng, S. Z. Gilani, Y. Wang, L. Zhang, and A. Mian, "Relation graph network for 3d object detection in point clouds," *IEEE Transactions on Image Processing*, vol. 30, pp. 92–107, 2020.
- [22] S. Shi, C. Guo, L. Jiang, Z. Wang, J. Shi, X. Wang, and H. Li, "Pv-rnn: Point-voxel feature set abstraction for 3d object detection," in *Proceedings of the IEEE/CVF conference on computer vision and pattern recognition*, 2020, pp. 10 529–10 538.
- [23] J. Deng, S. Shi, P. Li, W. Zhou, Y. Zhang, and H. Li, "Voxel r-cnn: Towards high performance voxel-based 3d object detection," in *Proceedings of the AAAI conference on artificial intelligence*, vol. 35, no. 2, 2021, pp. 1201–1209.
- [24] H. Wu, C. Wen, W. Li, X. Li, R. Yang, and C. Wang, "Transformation-equivariant 3d object detection for autonomous driving," in *Proceedings of the AAAI Conference on Artificial Intelligence*, vol. 37, no. 3, 2023, pp. 2795–2802.
- [25] Y. Zhang, Q. Zhang, Z. Zhu, J. Hou, and Y. Yuan, "Glenet: Boosting 3d object detectors with generative label uncertainty estimation," *International Journal of Computer Vision*, vol. 131, no. 12, pp. 3332–3352, 2023.
- [26] C. Yu, B. Peng, Q. Huang, and J. Lei, "Pipe-3ddet: Harnessing perspective information and proposal correlation for 3d point cloud object detection," *IEEE Transactions on Circuits and Systems for Video Technology*, 2023.
- [27] J.-K. Lee, J.-H. Lee, J. Lee, S. Kwon, and H. Jung, "Re-voxeldet: Rethinking neck and head architectures for high-performance voxel-based 3d detection," in *Proceedings of the IEEE/CVF Winter Conference on Applications of Computer Vision*, 2024, pp. 7503–7512.
- [28] B. Fan, K. Zhang, and J. Tian, "Hcpvf: Hierarchical cascaded point-voxel fusion for 3d object detection," *IEEE Transactions on Circuits and Systems for Video Technology*, 2023.
- [29] W. Xiao, Y. Peng, C. Liu, J. Gao, Y. Wu, and X. Li, "Balanced sample assignment and objective for single-model multi-class 3d object detection," *IEEE Transactions on Circuits and Systems for Video Technology*, vol. 33, no. 9, pp. 5036–5048, 2023.
- [30] Q. Cai, Y. Pan, T. Yao, and T. Mei, "3d cascade rcnn: High quality object detection in point clouds," *IEEE Transactions on Image Processing*, vol. 31, pp. 5706–5719, 2022.
- [31] L. Xie, G. Xu, D. Cai, and X. He, "X-view: Non-egocentric multi-view 3d object detector," *IEEE Transactions on Image Processing*, vol. 32, pp. 1488–1497, 2023.
- [32] Y. Feng, S. Liu, and Y. Zhu, "Real-time spatio-temporal lidar point cloud compression," in *2020 IEEE/RSJ international conference on intelligent robots and systems (IROS)*. IEEE, 2020, pp. 10 766–10 773.
- [33] S. Wang and M. Liu, "Point cloud compression with range image-based entropy model for autonomous driving," in *European Conference on Computer Vision*. Springer, 2022, pp. 323–340.
- [34] S. Wang, J. Jiao, P. Cai, and L. Wang, "R-pcc: A baseline for range image-based point cloud compression," in *2022 International Conference on Robotics and Automation (ICRA)*. IEEE, 2022, pp. 10 055–10 061.
- [35] W. Zimmer, R. Pranamulia, X. Zhou, M. Liu, and A. C. Knoll, "Pointcompress3d: A point cloud compression framework for roadside lidars in intelligent transportation systems," 2024. [Online]. Available: <https://arxiv.org/abs/2405.01750>
- [36] Y. He, X. Ren, D. Tang, Y. Zhang, X. Xue, and Y. Fu, "Density-preserving deep point cloud compression," in *Proceedings of the IEEE/CVF*

Conference on Computer Vision and Pattern Recognition, 2022, pp. 2333–2342.

- [37] X. Cai, Y. Wang, Z. Huang, Y. Shao, and D. Li, “Voloc: Visual place recognition by querying compressed lidar map,” in *2024 IEEE International Conference on Robotics and Automation (ICRA)*. IEEE, 2024, pp. 10 192–10 199.
- [38] Z. Li, W. Wang, Z. Wang, and N. Lei, “Point cloud compression via constrained optimal transport,” in *2024 IEEE International Conference on Multimedia and Expo (ICME)*. IEEE, 2024, pp. 1–6.
- [39] L. Zhao, K.-K. Ma, Z. Liu, Q. Yin, and J. Chen, “Real-time scene-aware lidar point cloud compression using semantic prior representation,” *IEEE Transactions on Circuits and Systems for Video Technology*, vol. 32, no. 8, pp. 5623–5637, 2022.
- [40] L. Zhao, K.-K. Ma, X. Lin, W. Wang, and J. Chen, “Real-time lidar point cloud compression using bi-directional prediction and range-adaptive floating-point coding,” *IEEE transactions on broadcasting*, vol. 68, no. 3, pp. 620–635, 2022.
- [41] Q. Zhang, J. Hou, Y. Qian, Y. Zeng, J. Zhang, and Y. He, “Flattening-net: Deep regular 2d representation for 3d point cloud analysis,” *IEEE Transactions on Pattern Analysis and Machine Intelligence*, vol. 45, no. 8, pp. 9726–9742, 2023.
- [42] Y. Zeng, J. Hou, Q. Zhang, S. Ren, and W. Wang, “Dynamic 3d point cloud sequences as 2d videos,” *IEEE Transactions on Pattern Analysis and Machine Intelligence*, 2024.
- [43] Q. Zhang, J. Hou, Y. Qian, A. B. Chan, J. Zhang, and Y. He, “Reggeonet: Learning regular representations for large-scale 3d point clouds,” *International Journal of Computer Vision*, vol. 130, no. 12, pp. 3100–3122, 2022.
- [44] S. Gu, J. Hou, H. Zeng, H. Yuan, and K.-K. Ma, “3d point cloud attribute compression using geometry-guided sparse representation,” *IEEE Transactions on Image Processing*, vol. 29, pp. 796–808, 2020.
- [45] J. Yang, S. Shi, R. Ding, Z. Wang, and X. Qi, “Towards efficient 3d object detection with knowledge distillation,” *Advances in Neural Information Processing Systems*, vol. 35, pp. 21 300–21 313, 2022.
- [46] L. Zhang, R. Dong, H.-S. Tai, and K. Ma, “Pointdistiller: Structured knowledge distillation towards efficient and compact 3d detection,” in *Proceedings of the IEEE/CVF conference on computer vision and pattern recognition*, 2023, pp. 21 791–21 801.
- [47] Y. Li, S. Xu, M. Lin, J. Yin, B. Zhang, and X. Cao, “Representation disparity-aware distillation for 3d object detection,” in *Proceedings of the IEEE/CVF International Conference on Computer Vision*, 2023, pp. 6715–6724.
- [48] H. Zhang, L. Liu, Y. Huang, X. Lei, L. Tong, and B. Wen, “Instkd: Towards lightweight 3d object detection with instance-aware knowledge distillation,” *IEEE Transactions on Intelligent Vehicles*, 2024.
- [49] H. Cho, J. Choi, G. Baek, and W. Hwang, “itkd: Interchange transfer-based knowledge distillation for 3d object detection,” in *Proceedings of the IEEE/CVF Conference on Computer Vision and Pattern Recognition*, 2023, pp. 13 540–13 549.
- [50] Z. Chen, Z. Chen, Z. Li, S. Zhang, L. Fang, Q. Jiang, F. Wu, and F. Zhao, “Graph-detr4d: Spatio-temporal graph modeling for multi-view 3d object detection,” *IEEE Transactions on Image Processing*, 2024.
- [51] B. Ju, Z. Zou, X. Ye, M. Jiang, X. Tan, E. Ding, and J. Wang, “Paint and distill: Boosting 3d object detection with semantic passing network,” in *Proceedings of the 30th ACM International Conference on Multimedia*, 2022, pp. 5639–5648.
- [52] A. Gambashidze, A. Dadukin, M. Golyadkin, M. Razzhivina, and I. Makarov, “Weak-to-strong 3d object detection with x-ray distillation,” in *Proceedings of the IEEE/CVF Conference on Computer Vision and Pattern Recognition*, 2024, pp. 15 055–15 064.
- [53] Y. Wei, Z. Wei, Y. Rao, J. Li, J. Zhou, and J. Lu, “Lidar distillation: Bridging the beam-induced domain gap for 3d object detection,” in *European Conference on Computer Vision*. Springer, 2022, pp. 179–195.
- [54] J. Shan, G. Zhang, C. Tang, H. Pan, Q. Yu, G. Wu, and X. Hu, “Focal distillation from high-resolution data to low-resolution data for 3d object detection,” *IEEE Transactions on Intelligent Transportation Systems*, vol. 24, no. 12, pp. 14 064–14 075, 2023.
- [55] X. Huang, H. Wu, X. Li, X. Fan, C. Wen, and C. Wang, “Sunshine to rainstorm: Cross-weather knowledge distillation for robust 3d object detection,” in *Proceedings of the AAAI Conference on Artificial Intelligence*, vol. 38, no. 3, 2024, pp. 2409–2416.



Hao Jing received the B.E. and M.E. degrees from the University of Science and Technology Beijing, China, in 2014 and 2017, respectively. He is currently pursuing the Ph.D. degree with Taiyuan University of Science and Technology, China. His research interests include 3D object detection and computer vision.



Anhong Wang received the B.S. and M.S. degrees from Taiyuan University of Science and Technology, China, in 1994 and 2002, respectively, and the Ph.D. degree from the Institute of Information Science, Beijing Jiaotong University (BJTU), in 2009. She became an Associate Professor with TYUST in 2005 and became a Professor in 2009. She is currently the Director of the Institute of Digital Media and Communication, Taiyuan University of Science and Technology. Her research interests include image coding, video coding, and visual intelligence.



Yifan Zhang received the B.E. degree from the Huazhong University of Science and Technology (HUST), the M.E. degree from Shanghai Jiao Tong University (SJTU), and the Ph.D. degree from the Department of Computer Science, City University of Hong Kong. Since 2025, he has been a lecturer at Shanghai University. His research interests include deep learning and 3D scene understanding.



Donghan Bu received the B.E. and M.E. degrees from Taiyuan University of Science and Technology, China, in 2017 and 2021, respectively, where she is currently pursuing the Ph.D. degree. Her research interests include 3D point cloud processing and computer vision.



Junhui Hou (Senior Member, IEEE) is an Associate Professor with the Department of Computer Science, City University of Hong Kong. He holds a B.Eng. degree in information engineering (Talented Students Program) from the South China University of Technology, Guangzhou, China, an M.Eng. degree in signal and information processing from Northwestern Polytechnical University, Xi’an, China, and a Ph.D. degree from the School of Electrical and Electronic Engineering, Nanyang Technological University, Singapore. His research interests are multi-dimensional visual computing.

Dr. Hou received the Early Career Award from the Hong Kong Research Grants Council in 2018 and the NSFC Excellent Young Scientists Fund in 2024. He has served or is serving as an Associate Editor for *IEEE Transactions on Visualization and Computer Graphics*, *IEEE Transactions on Image Processing*, *IEEE Transactions on Multimedia*, and *IEEE Transactions on Circuits and Systems for Video Technology*.